JGR Space Physics

RESEARCH ARTICLE
10.1029/2024JA032619

A Statistical Study of the Day-To-Day Variability of Diurnal and Semidiurnal Tides in the Ionospheric Dynamo Region From MIGHTI/ICON Observations

J. Oberheide[1], **X. Lu**[1], **and D. Aggarwal**[1]

[1]Department of Physics and Astronomy, Clemson University, Clemson, SC, USA

Key Points:

- Statistics of the day-to-day variability (DTDV) of diurnal and semidiurnal tides in the ionospheric dynamo region is obtained from Michelson Interferometer for Global High-Resolution Thermospheric Imaging/Ionospheric Connection Explorer
- DTDV is validated with COSMIC-2 ionospheric observations
- Statistics is extended to all latitudes using Hough Mode Extensions

Correspondence to:

J. Oberheide,
joberhe@clemson.edu

Citation:

Oberheide, J., Lu, X., & Aggarwal, D. (2024). A statistical study of the day-to-day variability of diurnal and semidiurnal tides in the ionospheric dynamo region from MIGHTI/ICON observations. *Journal of Geophysical Research: Space Physics*, *129*, e2024JA032619. https://doi.org/10.1029/2024JA032619

Received 8 MAR 2024
Accepted 26 JUN 2024

Author Contributions:

Funding acquisition: X. Lu
Investigation: X. Lu
Project administration: X. Lu
Resources: X. Lu
Validation: D. Aggarwal
Writing – review & editing: X. Lu, D. Aggarwal

Abstract The statistics of day-to-day tidal variability within 35-day running mean windows is obtained from Michelson Interferometer for Global High-Resolution Thermospheric Imaging (MIGHTI)/Ionospheric Connection Explorer (ICON) observations in the 90–107 km height region for the year 2020. Temperature standard deviations for 18 diurnal and semidiurnal tidal components, and for four quasi-stationary planetary waves are presented, as function of latitude, altitude, and day-of-year. Our results show that the day-to-day variability (DTDV) can be as large as 70% of the monthly mean amplitudes, thus providing a significant source of variability for the ionospheric E-region dynamo and hence for the F-region plasma. We further validate our results with COSMIC-2 ionospheric observations and present an approach to extend the MIGHTI/ICON results to all latitudes using Hough Mode Extension fitting, to produce global tidal fields and their statistical DTDV that are suitable as lower boundary conditions for nudging and ensemble modeling of TIE-GCM. In the future, this will likely help to establish a data-driven perspective of space weather variability caused by the tidal weather of the lower atmosphere.

1. Introduction

Upward propagating tides from the lower atmosphere are known to vary substantially from 1 day to another, due to weather-like variations in their tropospheric sources (Kumari & Oberheide, 2020; Wang et al., 2021), middle atmosphere processes like vortex strength variations (Oberheide, 2022; Pedatella & Harvey, 2022), interaction with planetary waves (Lieberman et al., 2004, 2015; Pedatella, Richmond, et al., 2016) and interaction with the mean flow when propagating upward (Pedatella, Oberheide, et al., 2016). See Lu et al. (2012) for a discussion of the relevant terms in the tidal momentum equations. Day-to-day tidal variability in the ionospheric E-region is a major driver of F-region plasma variability due to dynamo action and wave-driven circulation changes (Forbes et al., 2000; Mendillo et al., 2002). However, observing the day-to-day variability (DTDV) of the tidal spectrum in the E-region remains a challenge and our current understanding largely relies on modeling. Most tidal wave power is in zonal wavenumbers ≤ 6 (Forbes et al., 2008; Oberheide et al., 2006) which can only be diagnosed from satellite data due to the lack of ground-based observations over the oceans, with notable exceptions in Antarctica where the semidiurnal spectrum has been diagnosed from meteor radar observations (Murphy et al., 2003). A major hurdle for spaceborne tidal diagnostic on a day-to-day basis is the requirement to have measurements at a minimum of six local solar times (LST) per day every 4 hr to resolve the diurnal and semidiurnal tidal spectrum and the mean state (Oberheide, Jones, & Kumari, 2023). Hence, satellite constellations of at least three spacecraft in suitable orbits with instruments that are day- and nighttime capable are needed. At present, such constellations only exist for electron density measurements from the COSMIC-2 constellation, providing Global Ionospheric Specifications (GIS) with 1 hr time resolution (Lin et al., 2020; Rajesh et al., 2021). No complement for neutral dynamics measurements exists and the heliophysics community has to await forthcoming missions such as the Geospace Dynamics Constellation that will be able to resolve day-to-day tidal variability in the upper part of the thermosphere (Oberheide, Gardner, & Neogi, 2023).

To overcome the lack of LST resolution, a number of alternative methods have been developed to assess day-to-day tidal temperature and wind variability from space. All of these approaches, however, make certain assumptions (i.e., neglecting parts of the tidal spectrum) or are constrained to special cases that limit their scope and what tidal components can be analyzed (Dhadly et al., 2018; Kumari & Oberheide, 2020; Lieberman et al., 2015; Oberheide et al., 2015; Pedatella, Oberheide, et al., 2016). In this paper, we study the problem from a different perspective by focusing on the statistics of day-to-day tidal variability in temperature based on measurements made by the Michelson Interferometer for Global High-Resolution Thermospheric Imaging (MIGHTI) instrument on-board the

Ionospheric Connection Explorer (ICON) satellite (Englert et al., 2023; Harding et al., 2021). We also performed a similar analysis for tidal winds from MIGHTI and found consistent results with temperature. For readability, we focus on temperature in the following and only show one result for the zonal wind in Section 3.

For the year 2020 and from 90 to 103 km, we compute temperature standard deviations within 35-day running mean windows for 18 diurnal and semidiurnal tidal components, for four quasi-stationary planetary waves (QSPW), and for the mean as function of latitude, altitude, and day-of-year (DOY). By applying Hough Model Extension (HME) fitting, we further extend the results to all latitudes to obtain global tidal fields and their standard deviations that are suitable as lower boundary conditions for future ensemble modeling of tidal coupling into the electrodynamics. When comparing our E-region results with F-region day-to-day tidal variability derived from COSMIC-2 electron densities, we find good agreement for F-region tides that are driven by E-region dynamo, especially the much studied DE3 tidal component. This indicates that the tidal "weather" of the lower thermosphere directly impacts the space weather of the F-region ionosphere on a day-by-day basis.

The manuscript is organized as follows. Section 2 describes the methodology to obtain the statistical DTDV of the tides and QSPW, from pole-to-pole, and throughout the ionospheric dynamo region. This is done with some level of details since a comparable diagnostic has not been reported before in the literature. Section 3 validates the approach for the well-studied DE3 nonmigrating tide by comparing with ionospheric diagnostics of COSMIC-2 radio occultation data. Section 4 discusses the seasonal variation of the DTDV and Section 5 are the conclusions.

2. Data and Methodology

2.1. MIGHTI/ICON

MIGHTI is the instrument onboard the ICON spacecraft that measures winds and temperatures in the mesosphere/lower thermosphere from atomic oxygen green line airglow emissions. Englert et al. (2023) review the on-orbit performance and data analysis focused on the MIGHTI data release version 5 data (temperature and winds) we use in this manuscript. Due to the low inclination of ICON (27°) and MIGHTI looking to the left (with respect to the flight direction), the latitudinal coverage is limited to latitudes between 12°S and 42°N, with a data gap when the spacecraft is in the South Atlantic Anomaly. With its two viewing directions perpendicular to each other (called channels A and B), MIGHTI measures height profiles of temperature (called temperature-A and temperature-B) and vector winds (zonal and meridional winds) by combining the line-of-sight winds from each channel. For tidal diagnostics, the availability of day- and nighttime data is essential. Due to the lack of a green line signal at altitudes above 109 km during nighttime, the MIGHTI temperatures from channel A we use in the following are limited to 90–107 km. In this height range, MIGHTI measures at two different LST each day for a given latitude, separated by about 8 hr at 20°N. The LSTs on the ascending and descending parts of the orbit are largely independent of longitude (at given latitude). This is due to the precession rate of ICON which is −29.8 min/day (−12 hr/27 days). Ascending orbit nodes are the part of the orbits when the spacecraft is moving northward and descending orbit nodes are the part of the orbits when the spacecraft is moving southward. Overall, full (24 hr) LST coverage is obtained after 41 days at all latitudes (Cullens et al., 2020). However, for all practical purposes 35 days are sufficient if one stays away 5° from the southernmost/northernmost latitudes.

2.2. 35-Day Composite Day Tidal Spectra

To derive the tidal spectrum (amplitudes and phases), we first average 35 days of observations into a composite day (24 hr LST coverage) as a function of latitude and altitude and then apply a two-dimensional Fourier approach, as exemplified in Figure 1. The required gridding is performed using harmonic fits in longitude and LST for each latitude and altitude, and the whole approach is stepped forward 1 day at a time. All amplitudes and phases in the remainder of this manuscript thus represent 35-day averages. The (longitude × latitude × local solar time) grid we use is (5° × 5° × 1 hr). Diagnosing tides over composite days is fairly standard and follows tidal temperature diagnostics from satellite instruments such as HRDI, SABER, TIDI, MIGHTI (Forbes et al., 2008, 2022; Khattatov et al., 1997; Oberheide et al., 2006, 2007; Yamazaki et al., 2023). Two-dimensional Fourier fitting of the gridded data provides the amplitudes $A_{n,s}$ and phases $\Phi_{n,s}$ in the LST frame. For zonal wavenumber $s \geq 0$, $n = [0, \pm1, \pm2, \pm3, \ldots]$, $\omega_n = n\omega_1$, $\omega_1 = 2\pi/24$ hr^{-1}, longitude λ and t_{LST} as LST in hours, the observed signal is expressed as

$$\sum_{n,s} A_{n,s} \cos((s+n)\lambda - \omega_n t_{LST} - \Phi_{n,s}) \quad (1)$$

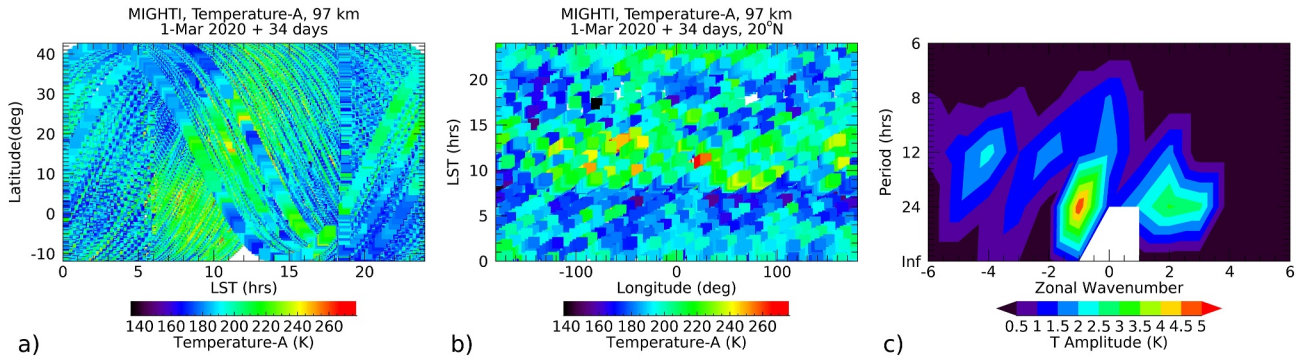

Figure 1. (a) All Michelson Interferometer for Global High-Resolution Thermospheric Imaging (MIGHTI) temperature measurements at 97 km from channel A as function of local solar time and latitude, for the 35-day window starting on 1 March 2020. (b) Same as (a) but for 20°N latitude (±2.5°) and as function of longitude and local solar time. (c) Resulting 35-day mean amplitude spectrum at 20°N with center (composite) day-of-year 78 (March 18). Negative (positive) zonal wavenumbers indicate westward (eastward) propagation. The mean temperature is omitted.

with negative (positive) ω_n indicating westward (eastward) propagation. In the altitude region of interest, only $|n| \leq 2$ (mean, QSPW, diurnal tides, semidiurnal tides) matter (Forbes et al., 2008). Note that a number of different (s, n) combinations would be observed as the same apparent zonal wavenumber $|s + n|$ when observed at constant LST. For example, $(s, n) = (1, -1)$ would result in $s + n = 0$, and so would $(s, n) = (2, -2)$ and the mean state $(s, n) = (0, 0)$. Similarly, $s + n = |1|$ can be achieved through $(s, n) = (1, 0)$, $(s, n) = (1, -2)$, $(s, n) = (2, -1)$, $(s, n) = (2, -3)$. This will become important in the statistical approach described in Section 2.3.

To identify each tidal component (s, n), we follow standard nomenclature and in the following use a two letter, one number code that indicates period ("D": diurnal, "S": semidiurnal), propagation direction ("W": westward, "E": eastward), and zonal wavenumber. DW1 would be the diurnal westward propagating tide with zonal wavenumber 1 $(s, n) = (1, -1)$, SE2 would be the semidiurnal eastward propagating tide of zonal wavenumber 2 $(s, n) = (2, 2)$, and so on.

Deriving a quantitative measure of DTDV of the tides is done using a statistical approach that provides amplitude standard deviations for each of the 35-day composite days, for each tidal component. The overall approach can be broken down into two parts. First, standard deviations of observed zonal wavenumbers $|s + n| = 0, 1, 2, 3, 4$ are obtained (35-day window, as function of latitude and altitude, Section 2.3). These standard deviations are then, in the second part, distributed (branched) into the underlying diurnal, semidiurnal, and quasi-stationary wave components (Section 2.4).

2.3. Statistical DTDV Approach I: Standard Deviations of Observed Zonal Wavenumbers 0–4

The individual steps are as follows, with steps 1–4 exemplified in Figure 2, and step 5 in Figures 3 and 4.

Step 1. For given latitude and altitude, produce Hovmoeller diagrams for the observed temperatures T, over 35-day, for ascending and descending orbit nodes separately (Figures 2a and 2e).

Step 2. Do wave-0 to wave-4 fits for each day, as 3-day running mean to better handle missing data (Figures 2b and 2f). The DTDV includes variability imposed by LST changes from 1 day to another and DTDV due to changing waves (the DTDV we are interested in). The comparison of Figures 2a, 2b, 2e, and 2f indicates that limiting the fits to observed zonal wavenumbers $|s + n| \leq 4$ is sufficient because all salient large-scale features are reproduced. Adding higher wavenumbers $|s + n| = 5, 6$ did not result in substantial changes at latitudes poleward of 15°N but made the fits worse at lower latitudes due to the MIGHTI data gap when the spacecraft is in the South Atlantic Anomaly.

Step 3. Take the 35-day composite day tidal diagnostics of MIGHTI (Section 2.2) and reconstruct wave-0 to wave-4 in the Hovmoeller diagrams (Figures 2c and 2g) using the correct LST for each DOY and orbit node. The reconstruction includes the mean, QSPW, diurnal tides and semidiurnal tides. The reconstructed DTDV is only due to LST changes from 1 day to another because the amplitudes and phases used for the reconstruction are constant for a composite day.

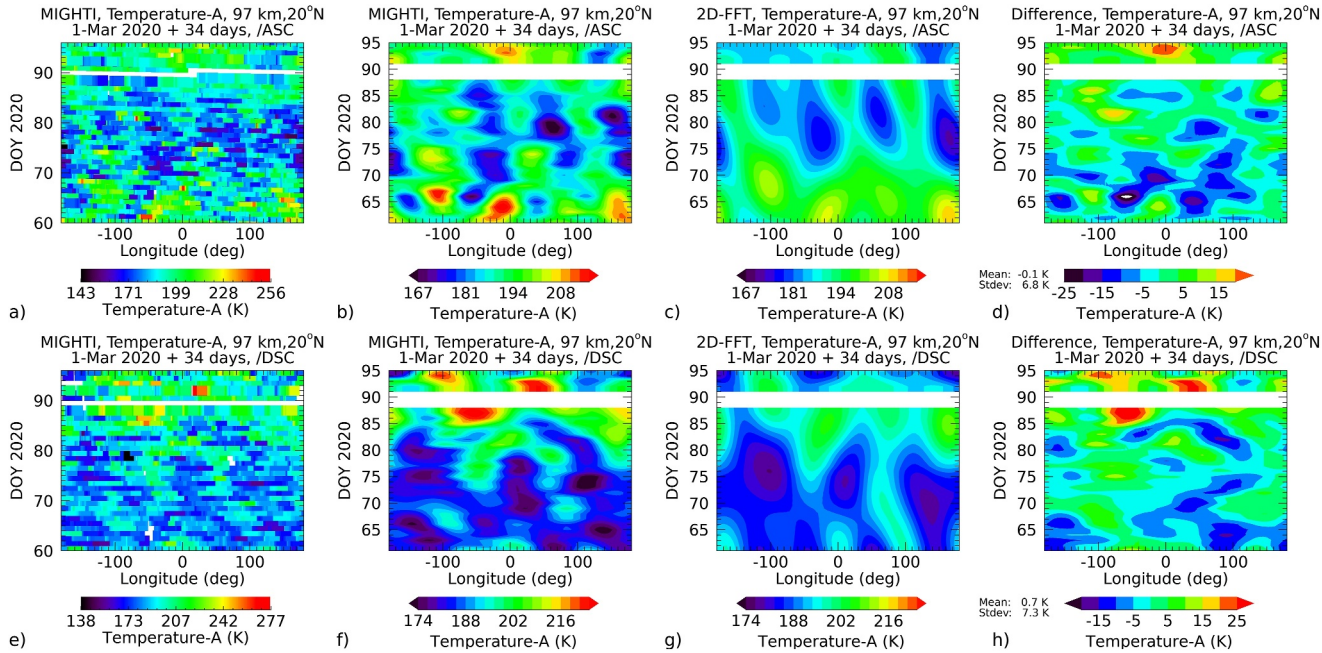

Figure 2. (a) Hovmoeller diagrams of all Michelson Interferometer for Global High-Resolution Thermospheric Imaging (MIGHTI) temperature measurements at 97 km and 20°N from channel A taken on the ascending orbit nodes as function of longitude and day-of-year (DOY), for the 35-day window starting on 1 March 2020. (b) Superposed wave-0 to wave-4 fits of (a). (c) Reconstructed wave-0 to wave-4 using the composite amplitudes and phases for this 35-day window. (d) Difference (b) and (c). Panels (e)–(h) are the same as (a)–(d) but for the descending orbit nodes. The white horizontal lines in each panel indicate a data gap around DOY 90.

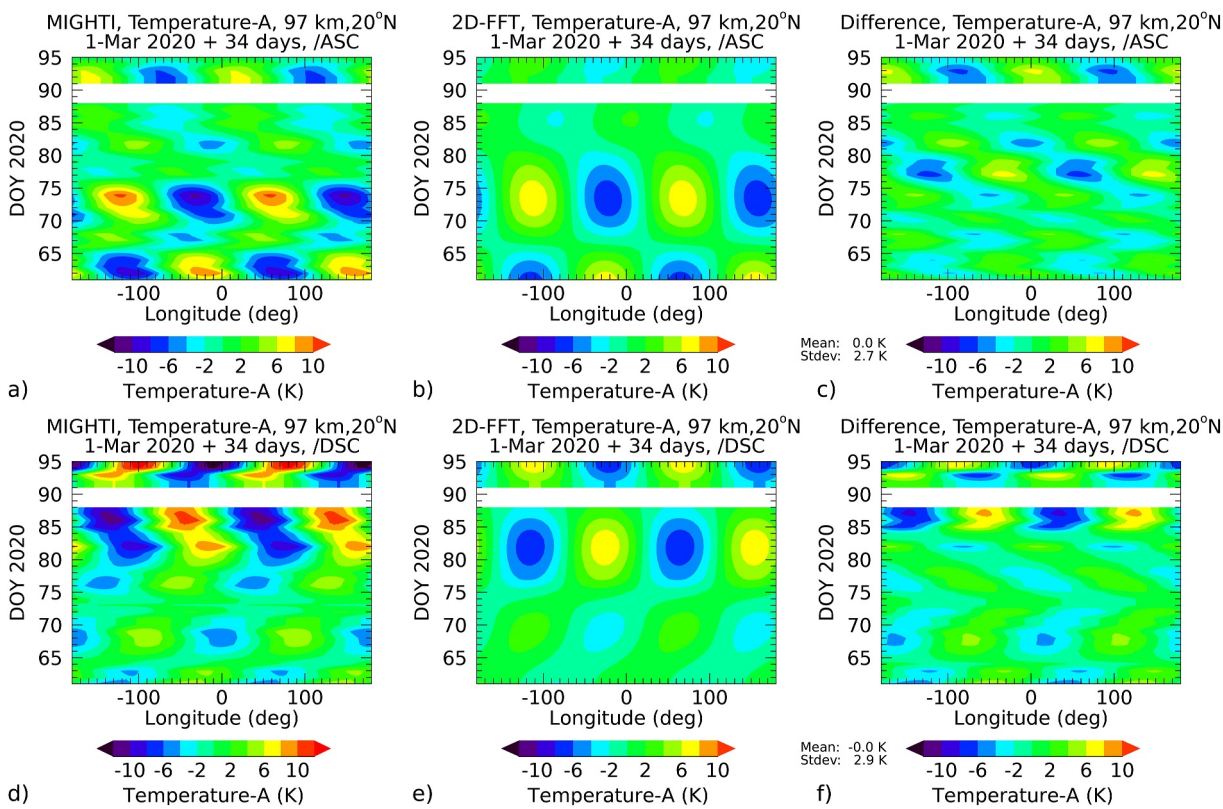

Figure 3. As Figure 2 (right three columns) but for $|s + n| = 2$ (wave-2) fits only. Wave-2 is a superposition of QSPW-2, DW3, DE1, SW4, S0.

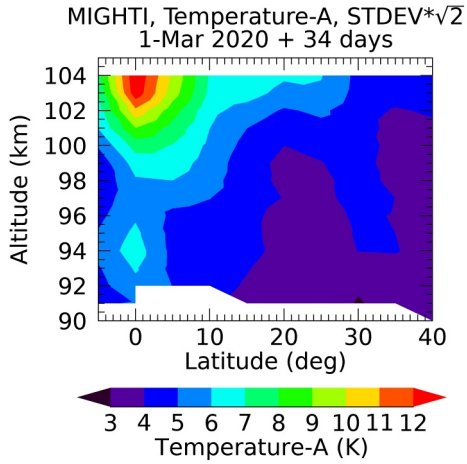

Figure 4. Averaged ascending and descending orbit node standard deviations multiplied by $\sqrt{2}$ (day-to-day variability) for observed zonal wavenumber $|s + n| = 2$ (wave-2) as function of latitude and altitude. Shown is the 35-day window starting on 1 March 2020.

Step 4. Compute differences between steps 2 and 3 (Figures 2d and 2h). This removes DTDV due to LST changes. Day-to-day variations in the differences are only due to changing waves. Mathematically, this can be expressed by rewriting Equation 1 for a given DOY using trigonometric identities and the mean amplitudes and phases from Section 2.2 as

$$\sum_{n,s}\left[(a_{n,s}-\bar{a}_{n,s})\cos((s+n)\lambda-\omega_n t_{LST})+\left(b_{n,s}-\bar{b}_{n,s}\right)\sin((s+n)\lambda-\omega_n t_{LST})\right] \quad (2)$$

with $a_{n,s} = A_{n,s}\cos(\Phi_{n,s})$, $b_{n,s} = A_{n,s}\sin(\Phi_{n,s})$ and the horizontal bars indicating 35-day averages. Since all tides are harmonics of the solar day covered within each 35-day composite, the variances of the sine and cosine terms in Equation 2 are 1/2, respectively. Consequently, and with $\sigma^2_{a_{n,s}}$ and $\sigma^2_{b_{n,s}}$ denoting the variances of $a_{n,s}$ and $b_{n,s}$, the variance from each (s, n) pair is then $\left(\sigma^2_{a_{n,s}} + \sigma^2_{b_{n,s}}\right)/2$.

In our previous work using tidal "deconvolution" approaches (Oberheide et al., 2015; Pedatella, Oberheide, et al., 2016), we found that day-to-day phase variability is quite small. The standard deviation of the differences expressed in Equation 2 is thus the desired measure (an upper bound if phase variability is present) of observed amplitude DTDV within a 35-day composite day. Specifically, the DTDV is the standard deviation $\sqrt{\sigma^2_{a_{n,s}} + \sigma^2_{b_{n,s}}}$ of the tidal amplitudes $A_{n,s} = \sqrt{a^2_{n,s} + b^2_{n,s}}$, or $\sqrt{2}$ times the observed standard deviation of Equation 2 or Figures 2d and 2h. It includes variability due to the mean, QSPWs and tides. The mean of the differences are always close to zero for both the ascending and descending orbit nodes and the standard deviations of both orbit nodes are always very similar which gives confidence into the approach as the ascending and descending orbit node LST dependence should be removed in Figures 2d and 2h, from a statistical perspective.

Step 5. Repeat steps 2 to 4 but for individual wavenumbers. For example, the standard deviation for observed wavenumber $|s + n| = 2$ shown in Figure 3 is 2.7 K for the ascending orbit node and 2.9 K for the descending orbit node. That ascending and descending orbit nodes show almost the same standard deviation is a typical result for all $|s + n|$, latitudes, and altitudes. In the following, averaged ascending and descending orbit node standard deviations multiplied by $\sqrt{2}$ will be used, as a measure for the DTDV. Figure 4 shows this as a latitude/height cross-section for observed wavenumber $|s + n| = 2$ for the 35-day window starting on 1 March 2020, with increasing DTDV toward higher altitudes and generally decreasing DTDV toward middle latitudes. Figure 5 is the DTDV for observed wavenumbers 0 to 4 as a function of latitude and DOY at 97 km. Each DOY refers to the center day of a 35-day composite day. Overall, the derived DTDV is most pronounced around solstices and low latitudes. The wave-0 DTDV is a combination of mean, DW1, SW2; wave-1 of QSPW-1, DW2, D0, SW3, SW1; wave-2 of QSPW-2, DW3, DE1, SW4, S0; wave-3 of QSPW-3, DW4, DE2, SW5, SE1; wave-4 of QSPW-4, DW5, DE3, SW6, SE2.

The MIGHTI statistical "noise" uncertainty is provided in the data files (see open research statement) and is on order 1 K in the altitude range of interest. Both the 35-day composite tidal diagnostics and the DTDV calculation use approximately 2,100 data points for each altitude and latitude bin (15 orbits per day, 2 data points per latitude bin per orbit node, 2 orbit nodes, 35 days = $15 \times 2 \times 2 \times 35 = 2{,}100$ points). Resulting contributions from MIGHTI noise errors to the 35-day standard deviations are thus on order $1/\sqrt{2{,}100}$ and negligible. The MIGHTI systematic uncertainty from the data files is an almost constant value of 3 K. In case the systematic uncertainty is a bias that is independent of day- or nighttime conditions, such a bias would not impact tidal amplitudes and phases (only the mean). In case the bias is different for day- and nighttime conditions, it transforms into a "noise" error along time (but not longitude) for tidal diagnostic (too high for some local time, too low for some local time), introducing a bias/$\sqrt{2}$ amplitude error. The worst case scenario is thus a tidal amplitude error of 2 K. However, per MIGHTI data documentation, the systematic bias error largely comes from pre-flight filter position calibrations (day/night independent) such that the real systematic tidal amplitude error is likely to be smaller than 2 K. In terms

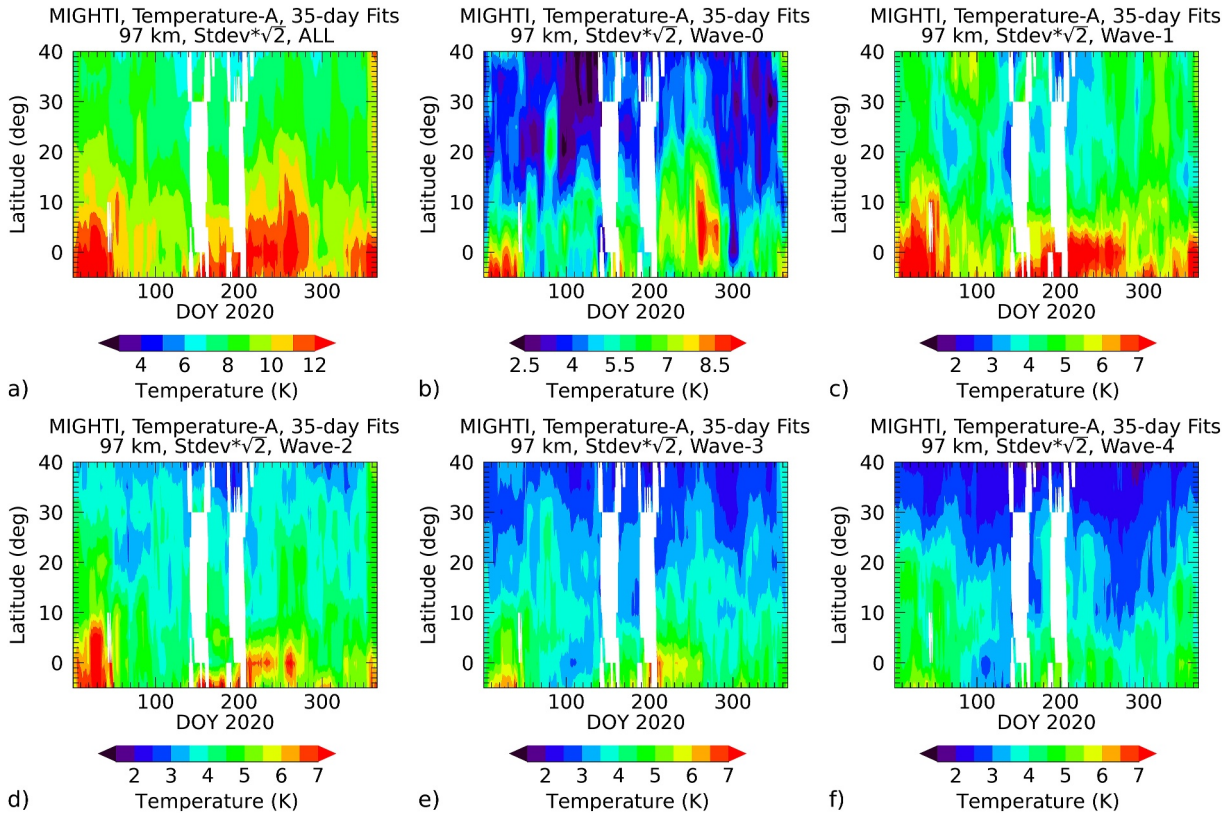

Figure 5. Averaged ascending and descending orbit node standard deviations multiplied by $\sqrt{2}$ (day-to-day variability) at 97 km altitude, as function of day-of-year and latitude. Note the partly different colorbars. (a) Wavenumbers 0–4 combined. (b) Wave-0. (c) Wave-1. (d) Wave-2. (e) Wave-3. (f) Wave-4. White areas indicate data gaps.

of standard deviations, a systematic amplitude error would add error/$\sqrt{2}$, hence a maximum of 1.4 K or more likely less than 1 K. Hence, both the statistical and systematic errors of the MIGHTI temperatures are not important contributors to the DTDV shown in Figure 5.

2.4. Statistical DTDV Approach II: Standard Deviations of Tidal Components

Standard deviations (multiplied by $\sqrt{2}$) of observed zonal wavenumbers like those shown in Figures 4 and 5 must now be separated into standard deviations of individual tidal components and QSPWs. This requires two more steps and uses the 35-day tidal spectra (Section 2.2) at each latitude and altitude.

Step 6. Compute the relative contributions (branching) of wave components into the observed wavenumbers 0–4 using the 35-day running mean amplitudes from the full tidal diagnostic. This is exemplified in Figure 6 for 97 km and the 35-day window starting on 1 March 2020. For example, the observed wave-2 is dominated by DE1 and SW4 (~30% each), followed by S0 (~20%), DW3 (~15%), and QSPW-2 (~5%). The sum of all contributions in each panel is 100%. Wave-0 has two contributions: DW1 and SW2 (assuming that the mean state does not contribute to wave-0 DTDV variability). Wave-1 to wave-4 have five contributions, respectively: two westward and two eastward propagating tides and one QSPW.

Step 7. Redistribute the standard deviations (multiplied by $\sqrt{2}$) from step 5 using the branching from step 6. These are then the desired DTDVs at the latitudes and altitude observed by MIGHTI/ICON, as exemplified for $|s+n|=2$ in Figure 7. The lower row DTDVs in Figure 7 (panels f–j) are computed by multiplying Figure 5d with the amplitude ratios in Figure 6c. The underlying assumption is that the tidal component DTDVs for a given observed wavenumber $|s+n|$ are independent from each other, that is, covariances between components such as DW5/DE3 etc. are zero. Consequently, the derived DTDV must be considered an upper bound. The DTDV for the tidal components around 97 km observed as $|s+n|=2$ is largely in the range of 0.5–0.7 relative to the observed

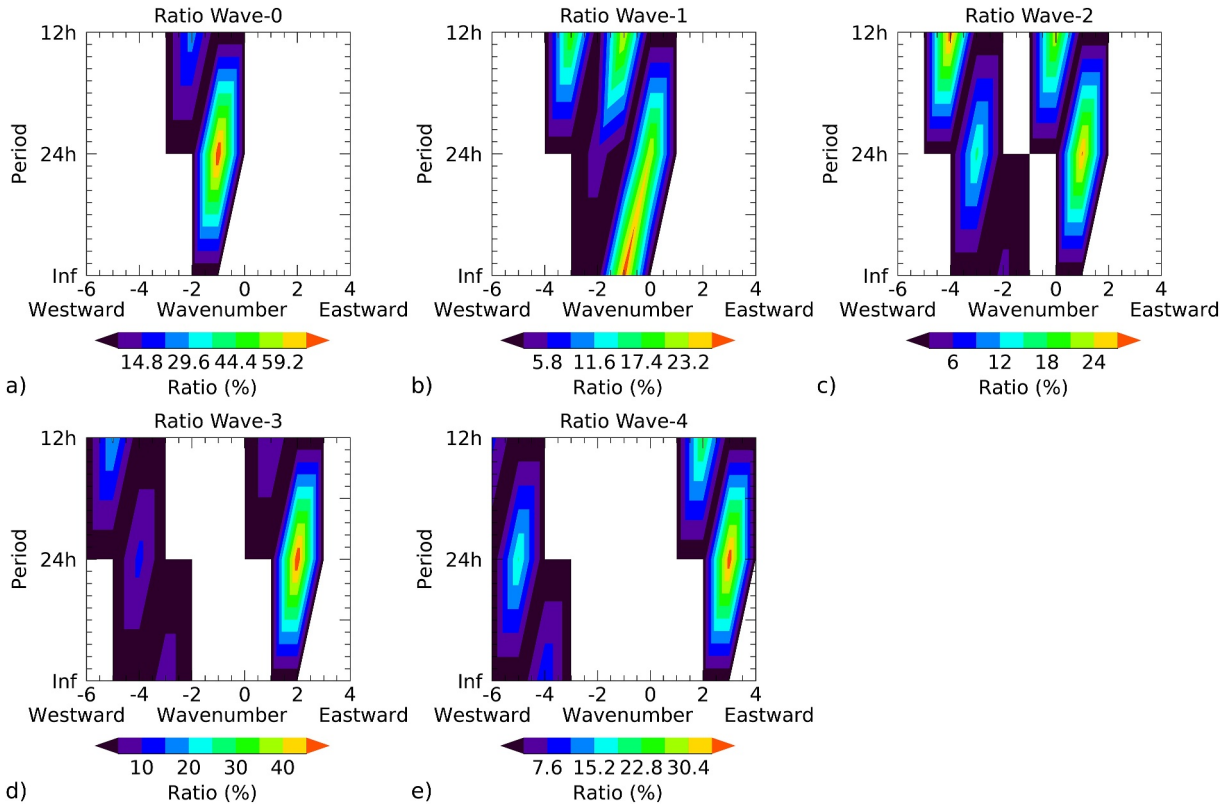

Figure 6. Amplitude ratios at 97 km altitude and 20°N for the 35-day window starting on 1 March 2020. Note the different colorbars. (a) Wave-0. (b) Wave-1. (c) Wave-2. (d) Wave-3. (e) Wave-4.

amplitudes throughout all seasons and latitudes. This is a fairly typical result for all observed wavenumbers although some differences exist (Figure 8). Furthermore, the approach of setting up the DTDV of each tidal component as amplitude times branching ratio results in the same relative DTDV (DTDV/amplitude) for of the tidal components (and QSPW) contributing to a particular observed zonal wavenumber $|s + n|$. The relative DTDV distributions as function of DOY and latitude in Figure 8 thus provide the complete picture at 97 km. The

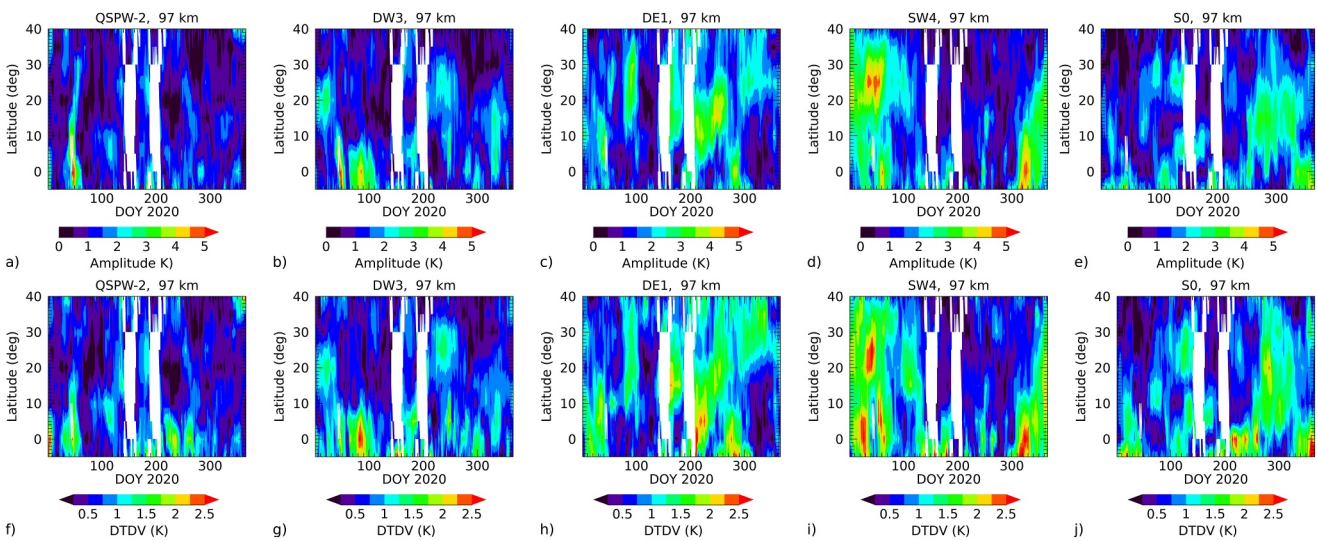

Figure 7. Amplitude (top row) and day-to-day variability (DTDV) (bottom row) at 97 km for observed zonal wavenumber $|s + n| = 2$ (wave-2), as function of day-of-year and latitude. (a, f) QSPW-2, (b, g) DW3, (c, h) DE1, (d, i) SW4, (e, j) S0.

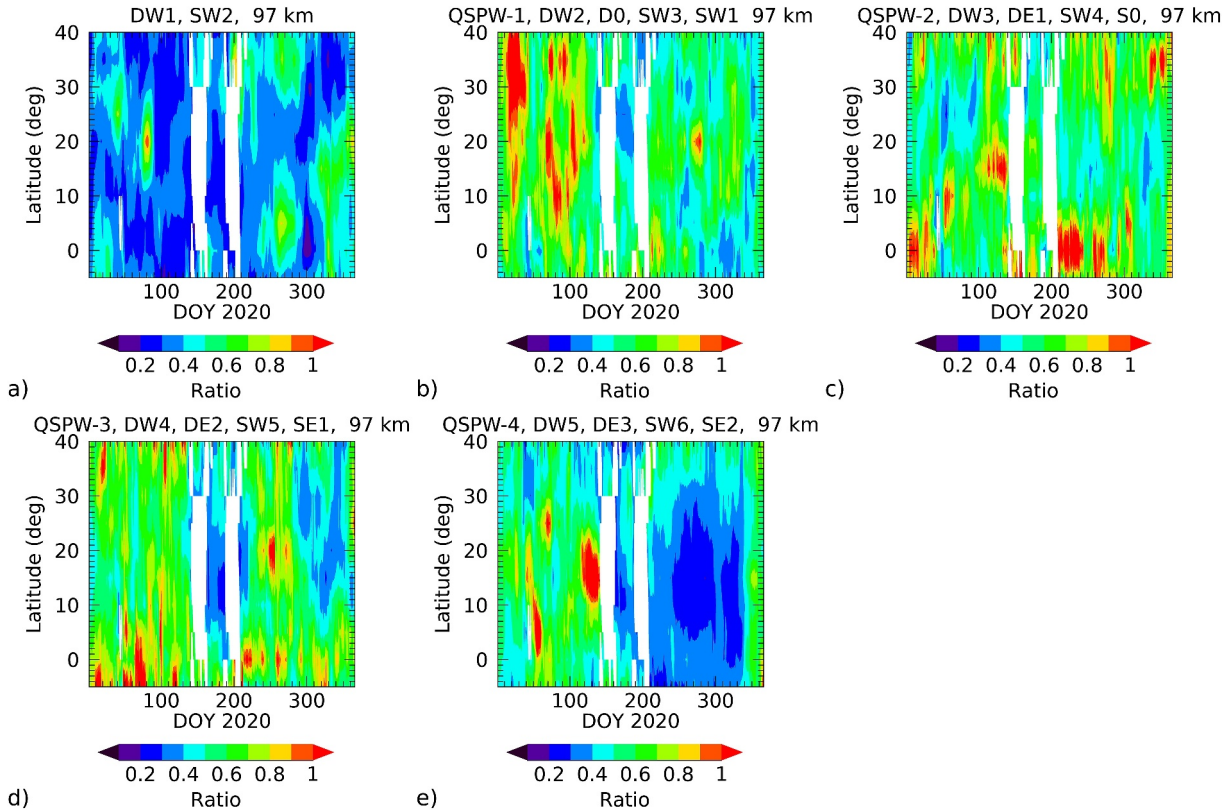

Figure 8. Relative day-to-day variability (DTDV) (DTDV to amplitude ratio) at 97 km, as function of day-of-year and latitude. (a) DW1, SW2, (b) QSPW-1, DW2, D0, SW3, SW1, (c) QSPW-2, DW3, DE1, SW4, S0, (d) QSPW-2, DW4, DE2, SW5, SE1, (e) QSPW-3, DW5, DE3, SW6, SE2.

largest ratios in Figure 8 (red areas) are always associated with small amplitudes. Larger amplitudes have ratios in the 0.5 to 0.7 range with only moderate latitude dependences. As such, one can use the latitude average of the relative DTDV as an overall measure for the DOY and height variation. This is shown in Figure 9. Clearly, the relative DTDV of the tidal components corresponding to different observed wavenumbers $|s + n| = 2$ exhibit quite different seasonal/height patterns. The reader is referred to Section 3 for further discussion.

2.5. Expanding DTDV Globally Using Hough Mode Extensions

We will now discuss an approach to extend the above results to all latitudes (pole-to-pole) with the goal to produce a lower boundary condition suitable for thermosphere-ionosphere-electrodynamics general circulation model (TIEGCM)-type models that not only provides the tidal fields but also the corresponding DTDV at all latitudes. The TIEGCM (Richmond et al., 1992; Roble et al., 1988) is a global 3D numerical model that simulates the coupled thermosphere/ionosphere system from ~97 to ~600 km. Among others, it solves the fully coupled, nonlinear, hydrodynamics thermodynamic and continuity equation. The lower boundary tidal and planetary wave field is either provided through other general circulation models such as TIME-GCM (Roble & Ridley, 1994) or SD-WACCMX (Liu et al., 2010), or linear models like GSWM (Hagan & Forbes, 2002), or empirical tidal models such as Climatological Tidal Model of the Thermosphere (CTMT) (Oberheide et al., 2011a). The latter is based on Hough Mode Extensions (HMEs; Lindzen et al., 1977) constrained by tidal temperature and wind diagnostics from TIMED observations. HME-based wave fields extend from pole-to-pole and into the upper thermosphere, with physically self-consistent (within the hydrodynamic equations) temperatures and winds. CTMT lower boundary conditions have been used to study the effect of upward propagating tides on the ionosphere-thermosphere using TIEGCM (Jones et al., 2014). A similar approach to drive TIEGCM has been applied using HMEs constrained with ICON tides (Maute et al., 2023). In the following we will build upon the previous work by adding DTDV to CTMT (or HME) based tidal fields.

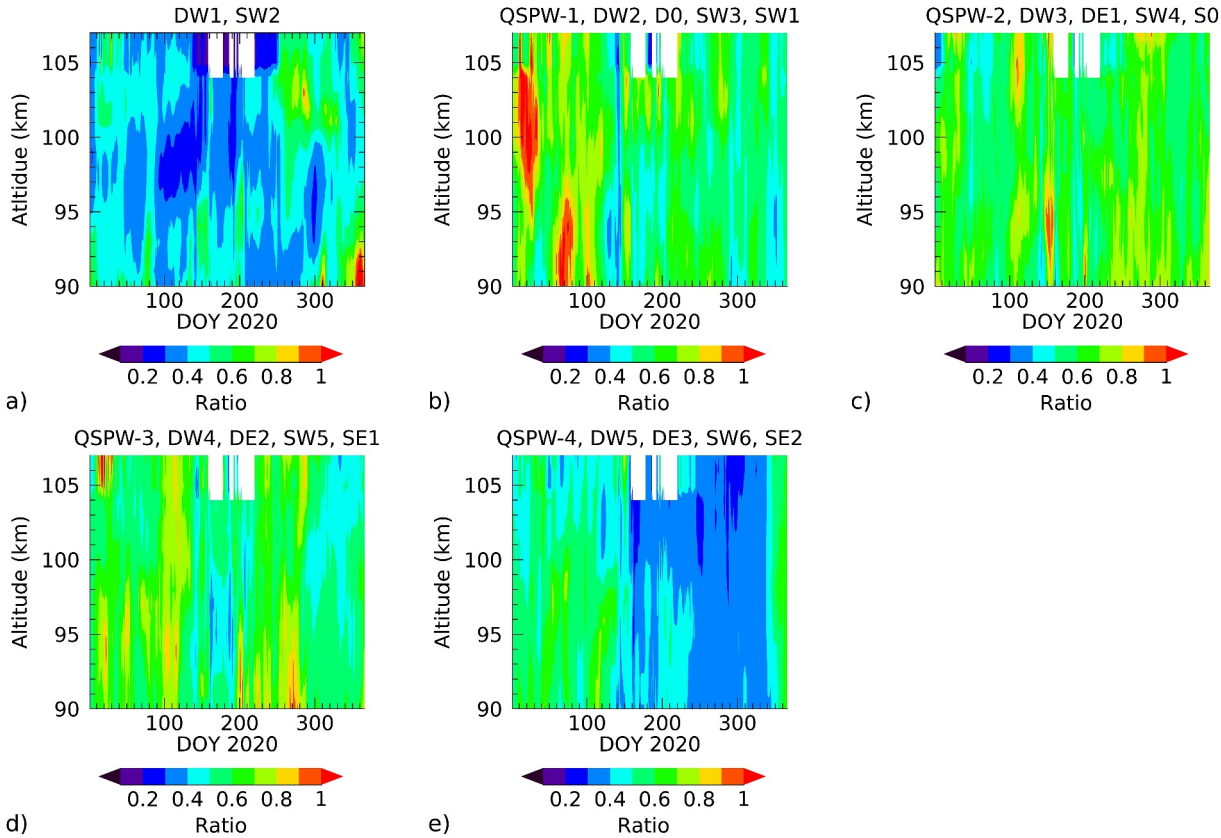

Figure 9. Latitude-averaged relative day-to-day variability (DTDV) (DTDV to amplitude ratio), as function of day-of-year and altitude. (a) DW1, SW2, (b) QSPW-1, DW2, D0, SW3, SW1, (c) QSPW-2, DW3, DE1, SW4, S0, (d) QSPW-3, DW4, DE2, SW5, SE1, (e) QSPW-4, DW5, DE3, SW6, SE2.

Briefly, HMEs are a way to incorporate dissipative processes into the classical tidal theory to study the latitude/height variation of tides that propagate upward from the lower parts of the atmosphere. Dissipation makes the classical tidal equations inseparable in latitude/height and numerical solutions are needed using a numerical model. In principle, HMEs can be thought of as a vector basis into which observed tides (amplitudes and phases) are projected by means of a least-squares fit. This points to a key characteristic of HMEs: fitting HMEs to observations in a limited latitude/height range still provides information (within the framework of the theory) about the tides at latitudes and height that are not observed. HMEs are global (pole-to-pole) and computed up to altitudes of 400 km (where tides have been transitioned into altitude independent amplitudes and phases due to molecular diffusion). We use the most recent set of HMEs provided by Forbes and Zhang (2022a) and the reader is referred to their work for further computational details. HMEs have been successfully used to analyze tides from Microwave Limb Sounder (MLS) on Upper Atmosphere Research Satellite (Forbes & Wu, 2006), SABER and TIDI on TIMED (Kumari & Oberheide, 2020; Oberheide & Forbes, 2008; Oberheide et al., 2011a) and MIGHTI/ICON (Forbes et al., 2022). The approach has been extensively validated with CHAMP (Forbes et al., 2009; Häusler et al., 2013), HRDI and WINDII (Lieberman et al., 2013) and ground-based observations (Lu et al., 2011; Yuan et al., 2014).

Figure 10 exemplifies the quality of the HME fits for the DE3 component. Note that Forbes and Zhang (2022a) provide HMEs for three different solar flux levels. We thus interpolate the HMEs to the daily mean solar flux for each day of the year before performing the fits. Fits were performed simultaneously to observed zonal winds, meridional winds, and temperature. The fitted amplitudes slightly (by 20%) overestimate the observed temperature amplitudes around 105 km. However, the fitted results reproduce the observed spatio-temporal variability very well, including phase structure and variability. HME fits can inherently close data gaps due to missing data at some latitudes or altitudes. Multiplying the fitted amplitudes with the latitude-averaged DTDV ratios from Figure 9 finally provide the global amplitude DTDV for DE3. The same approach can be done for all diurnal and semidiurnal components discussed above. It should, however, be emphasized that it will only be a data-based

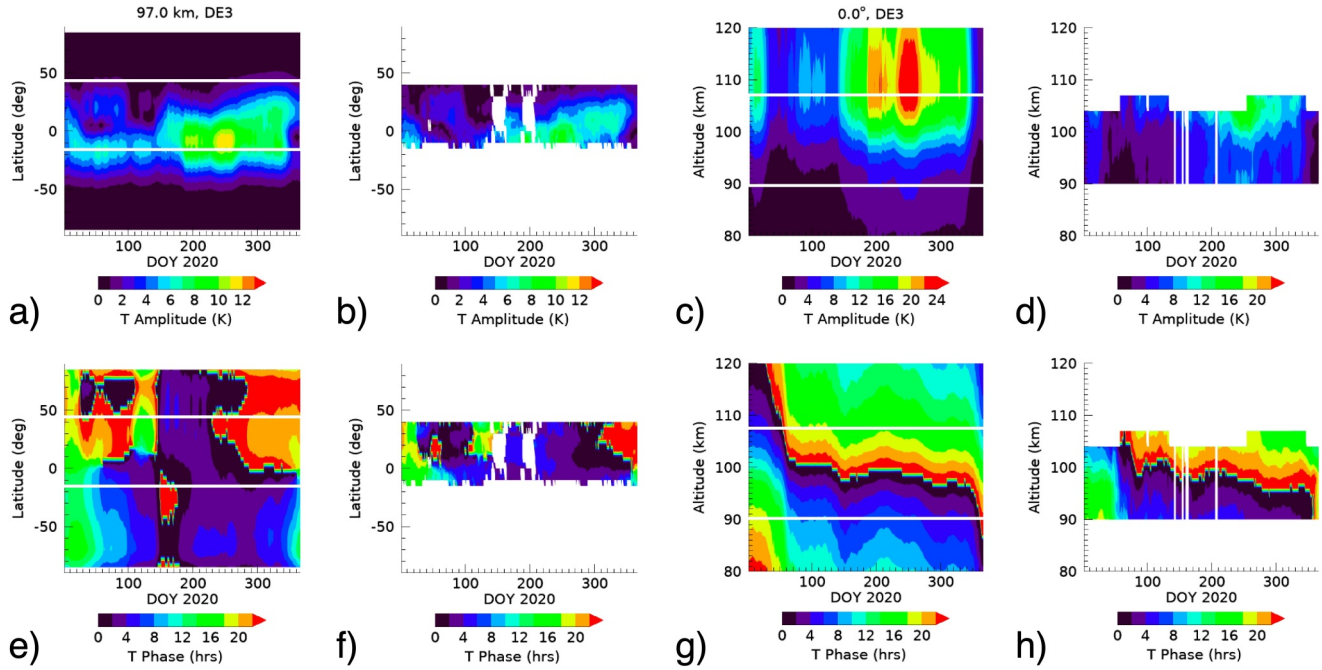

Figure 10. Fitted and observed temperature amplitudes (top row) and phases (bottom row) for the DE3 component. (a) Hough Model Extension (HME)-fitted amplitude as function of latitude and day-of-year (DOY) at 97 km altitude. The white lines indicate the observed altitude and latitude ranges. (b) Observed amplitude. (c) HME-fitted amplitude as function of DOY and altitude. (d) Observed amplitude. (e)–(h) Same but for phases (universal time of maximum at 0° longitude). White areas in the observed amplitudes and phases indicate data gaps.

proxy for the DTDV at all latitudes due to the involved limitations such as non-vanishing tidal component covariances and the DTDV ratio latitude-averaging.

3. Validation With COSMIC-2 Ionospheric Tides

Direct validation of the statistical DTDV approach has to await future global temperature and wind measurements with sufficient local solar time resolution to diagnose the tidal spectrum on a day-to-day basis (Oberheide, Jones, & Kumari, 2023). Nevertheless, an indirect validation can be done using electron density observations from the six satellite COSMIC-2 constellation that was launched in 2019, specifically from the COSMIC-2 GIS data product (Lin et al., 2020). COSMIC-2 observes slant total electron density (TEC) from radio occultation. GIS data are reconstructed 3D electron densities from slant TEC assimilated onto a 2.5° × 5° × 20 km × 1 hr (latitude × longitude × altitude × universal time) grid. Both COSMIC-2 and ground-based global positioning system data are assimilated such that GIS data have pole-to-pole coverage, between 120 and 700 km. Standard Fourier methods then allow one to derive the tidal spectrum on a daily basis in either geographic coordinates (Rajesh et al., 2021) or magnetic coordinates (Oberheide, 2022).

Day-to-day ionospheric tidal variability can be driven by E-region dynamo, F-region dynamo, thermospheric composition or solar driving, see for example, Forbes et al. (2000) or the review by Oberheide et al. (2015). However, the ionospheric signature of one particular and very well-studied tidal component has been conclusively linked to E-region dynamo driving (Pedatella et al., 2008): the diurnal eastward propagating nonmigrating tide of zonal wavenumber 3 (DE3) that has no known sources in the thermosphere. The comparatively simple latitude structure of the DE3 (resembling a long-vertical wavelength Kelvin wave structure in the E-region) without complicated modal superpositions above the mesopause (Oberheide et al., 2011b) makes it very effective for E-region dynamo coupling. This suggests that the statistical DTDVs of low latitude E-region DE3 zonal tidal winds and ionospheric DE3 electron densities in the equatorial ionization anomaly (EIA, 15° magnetic latitude) should be similar, at least on a seasonal timescale.

We therefore derived daily DE3 amplitudes from COSMIC-2 GIS data at 15°N magnetic latitude and computed their 35-day standard deviation. To minimize impacts from solar flux and/or geomagnetic activity, the COSMIC-2 standard deviations were computed from relative DE3 amplitudes, that is, DE3 electron density amplitude

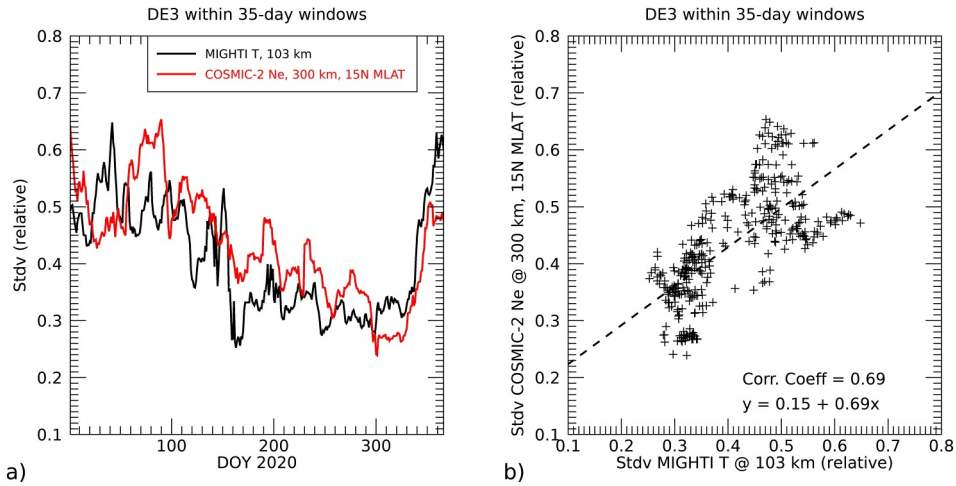

Figure 11. (a) Relative day-to-day variability (DTDV) for the DE3 component from Michelson Interferometer for Global High-Resolution Thermospheric Imaging temperatures at 103 km (black) and COSMIC-2 relative DE3 standard deviation at 15°N magnetic latitude and 300 km (red). (b) Scatterplot between DTDV and COSMIC-2 standard deviation with best linear fit and Pearson correlation coefficient.

divided by the zonal mean daily mean electron density for the same day, magnetic latitude and altitude. The comparison and correlation in Figure 11 shows that the seasonal cycle of the COSMIC-2 standard deviations closely follow the temperature DTDV at 103 km (the upper altitude of the MIGHTI temperature diagnostic without data gaps in 2020). Figure 12 shows the same comparison but now between DTDV from MIGHTI zonal winds (derived using the same method as detailed in Section 2) at 105 km altitude (the upper altitude of the MIGHTI wind diagnostic without data gaps in 2020). Again, the seasonal variation of DTDV in the E-region dynamo and the EIA ionospheric response agree well and we conclude that the COSMIC-2 data validate the seasonal characteristics of the derived statistical DTDV for the DE3 component. Seasonal or longer variations do not have a substantial impact on the COSMIC-2 standard deviations. Removing a 35-day running mean from the relative amplitudes before computing the standard deviations yielded almost identical results (Figure not shown).

It should be emphasized that direct correlations between the DTDV in the E-region and EIA tidal variability can not necessarily be expected for other tidal components, due to their generally more complex modal structure, thermospheric sources and possibly F-region dynamo effects. For example, we only found a weak correlation of 0.22 for the migrating semidiurnal tide (SW2). While a correlation coefficient of 0.22 is statistically significant, it clearly indicates that ionospheric SW2 variability is impacted by other effects, which is understandable since about half of the SW2 in the upper thermosphere originates in the thermosphere above the E-region dynamo

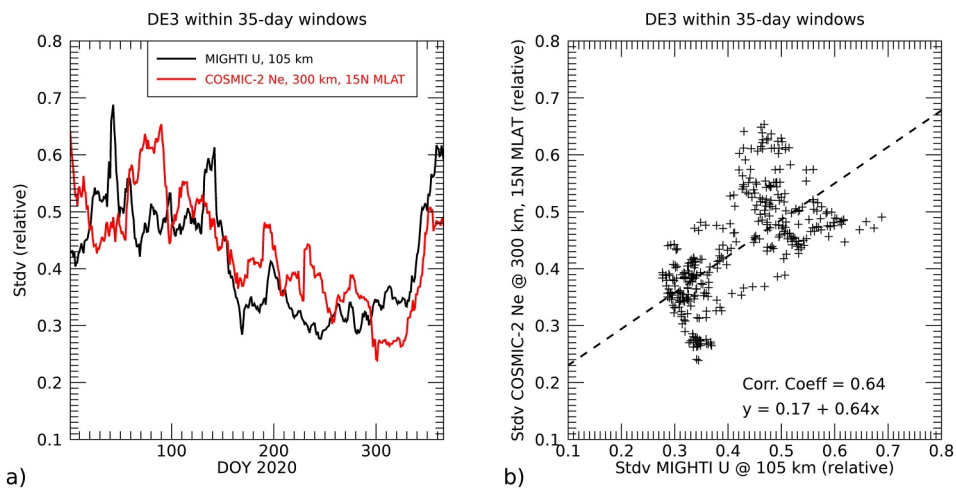

Figure 12. Same as Figure 11 but now for day-to-day variability in the zonal wind at 105 km.

(Forbes et al., 2011). Studying this complex behavior requires detailed modeling and data analysis efforts that are well beyond the scope of this paper, that is, driving TIEGCM with observed tides and their DTDV, and then comparing with observed tides from COSMIC-2 and possibly in-situ data from ICON.

4. Discussion

Comparatively few papers have attempted to study short-term tidal component variability due to the already mentioned local solar time requirements for global daily spectral analysis. Ground-based observations, on the other hand, are difficult to interpret due to tidal component interference. We will thus limit our discussion to the three components where low latitude variability has been analyzed before (DE3 and the two migrating tides DW1 and SW2) and check for consistency with our findings.

The seasonal variation of the DE3 DTDV (Figure 9) is consistent with the findings of Pedatella, Oberheide, et al. (2016) who used WACCM + DART simulations and SABER-based estimates to study the day-to-day tidal variability in the upper mesosphere/lower thermosphere for the year 2007. Relative model standard deviations at 100 km (as estimated from their Figure 1, 10-day running means) are on order 25% between DOY 150 and 350, and larger (up to 50%) during the remainder of the year. Pedatella, Oberheide, et al. (2016) concluded that there is no single point source of DE3 DTDV but that the majority of the DTDV could be attributed to changes in either tropospheric forcing or the zonal mean atmosphere (tidal upward propagation), with additional non-linear wave-wave interactions.

DW1 (migrating diurnal tide) short-term diagnostics have been performed by Wang et al. (2021) using combined year 2009 temperature data from SABER and MLS during days of the year when the local solar time coverage of the combined satellite data was favorable. At their upper analysis altitude of ∼80 km (10^{-2} hPa) and low latitudes, Wang et al. (2021) showed 3-month standard deviations of 10 K (January–March), 7 K (April–June) and 4–5 K (July–September, October–December). The corresponding 3-month averages of our 35-day running mean standard deviations at the equator and 90 km (the lowest altitude of our MIGHTI diagnostic) are 4.9 K (January–March), 4.1 K (April–June), 4.5 K (July–September), 3.5 K (October–December). These values are lower than reported by Wang et al. (2021) which can only partly be explained by the different altitudes and diagnosing a different year. However, our reported DTDV is based on 3-day running means and Wang et al. (2021) include tidal variability from 1 day to another. While tidal variations from 1 day to another pose analysis and interpretation challenges on their own, that is, tides are assumed to be constant over 24 hr and are then allowed to jump to another state, this could explain a $\sqrt{3}$ difference. Furthermore, the MIGHTI-based DTDV for DW1 is consistent with the 3-month standard deviations from NOGAPS-ALPHA and WACCM-X reported in the same paper, and we refer the reader to the explanation of the DW1 DTDV given by Wang et al. (2021), as a combination of some planetary wave/tidal interaction but mainly of tidal/gravity wave interactions throughout the year. Short-term (<30 days) DW1 variability from statistical eCMAM30 modeling is also on order 2–3 K at low latitudes (Vitharana et al., 2019), consistent with our findings.

Little is known about SW2 (migrating semidiurnal tide) short-term variability from observations. A notable exception is the TIDI-based diagnostic of Dhadly et al. (2018) which resulted in a multi-year mean DTDV of mesosphere/lower thermosphere SW2 meridional wind of 18 m/s at the equator (their Figure 8d). The corresponding MIGHTI meridional wind SW2 DTDV at the equator and 97 km altitude is 10 m/s (2020 average) which is about a factor of two smaller than the TIDI result. Whether this is due to the fact that the Dhadly et al. (2018) value includes DTDV on time scales 1–60 days while our MIGHTI values include DTDV on time scale 3–35 days or due to other reasons (including interannual variability) is not clear.

5. Conclusion

Using a statistical approach combined with Hough Mode Extension fitting, we derived a statistical measure for DTDV tidal variability within 35-day windows from 2020 MIGHTI/ICON temperature observations in the mesosphere/lower thermosphere. Our approach is capable of producing global lower boundary conditions suitable for TIEGCM for 18 tidal components that are (a) global, (b) physically self-consistent within the tidal equations and (c) include DTDV variability. The latter should be considered a proxy due to inherent limitations such as vanishing tidal component covariances. Overall, our approach will allow one in the future to conduct

ensemble simulations for studying pre-conditioning effects of day-to-day tidal variability in the E-region on the space weather of the F-region ionosphere.

The DTDV is on order ∼50%–70% of the 35-day mean amplitudes for most nonmigrating tidal components and somewhat lower (∼30%–50%) for the migrating tides and the components observed as a zonal wavenumber 4. A comparison with the few existing observation-based diagnostics indicates that our DTDV for the migrating diurnal and semidiurnal tides is generally smaller than SABER/MLS and TIDI based results. Some of the differences may be due to the different time-averaging of the different methods. However, the observed seasonal variation of the DTDV for the DE3 nonmigrating compares well with independent F-region COSMIC-2 ionospheric tides in the EIA. This not only validates the approach but also shows that DTDV in the E-region has a substantial impact on the variability of the F-region. The complexity of the modal tidal structure and their efficiency for E-region dynamo makes a one-to-one mapping of DTDV unlikely outside of relatively simple, Kelvin-wave like tides like the DE3. Future dedicated ensemble model simulations and comparative analysis of COSMIC-2 (and potentially GOLD) data will be needed to elucidate the underlying processes.

Data Availability Statement

COSMIC-2 GIS data are publicly available after free registration at http://formosat7.earth.ncku.edu.tw/ (FORMOSAT-7/COSMIC-2 LASC and SWL Lab, 2024). Conversion into geomagnetic coordinates was performed using the Python wrapper for the Apex fortran library by Emmert et al. (2010) that can be downloaded from https://doi.org/10.5281/zenodo.1214206 (van der Meeren et al., 2023). MIGHTI/ICON version v05 temperature and winds were obtained from https://icon.ssl.berkeley.edu/Data/Data-Product-Matrix (ICON/MIGHTI Team, 2024). Hough Mode Extensions have been obtained from https://doi.org/10.5281/zenodo.7150798 (Forbes & Zhang, 2022b).

Acknowledgments
The authors acknowledge funding from the NSF through the ANSWERS program, award 2149695; and from NASA through the GOLD-ICON Guest Investigator and LWS programs, Grants 80NSSC22K0018 and 80NSSC22K1010.

References

Cullens, C. Y., Immel, T. J., Triplett, C. C., Wu, Y.-J., England, S. L., Forbes, J. M., & Liu, G. (2020). Sensitivity study for icon tidal analysis. *Progress in Earth and Planetary Science*, *7*(18), 18. https://doi.org/10.1186/s40645-020-00330-6

Dhadly, M. S., Emmert, J. T., Drob, D. P., McCormack, J. P., & Niciejewski, R. J. (2018). Short-term and interannual variations of migrating diurnal and semidiurnal tides in the mesosphere and lower thermosphere. *Journal of Geophysical Research: Space Physics*, *123*(8), 7106–7123. https://doi.org/10.1029/2018JA025748

Emmert, J. T., Richmond, A. D., & Drob, D. P. (2010). A computationally compact representation of Magnetic-Apex and Quasi-Dipole coordinates with smooth base vectors. *Journal of Geophysical Research*, *115*(A8), A08322. https://doi.org/10.1029/2010JA015326

Englert, C. R., Harlander, J. M., Marr, K. D., Harding, B. J., Makela, J. J., Fae, T., et al. (2023). Michelson Interferometer for Global High-Resolution Thermospheric Imaging (MIGHTI) on-orbit wind observations: Data analysis and instrument performance. *Space Science Reviews*, *219*(27), 27. https://doi.org/10.1007/s11214-023-00971-1

Forbes, J. M., Bruinsma, S. L., Zhang, X., & Oberheide, J. (2009). Surface-exosphere coupling due to thermal tides. *Geophysical Research Letters*, *36*(15), L15812. https://doi.org/10.1029/2009GL038748

Forbes, J. M., Oberheide, J., Zhang, X., Cullens, C., Englert, C. R., Harding, B. J., et al. (2022). Vertical coupling by solar semidiurnal tides in the thermosphere from ICON/MIGHTI measurements. *Journal of Geophysical Research: Space Physics*, *127*(5), e2022JA030288. https://doi.org/10.1029/2022JA030288

Forbes, J. M., Palo, S. E., & Zhang, X. (2000). Variability of the ionosphere. *Journal of Atmospheric and Solar-Terrestrial Physics*, *62*(8), 685–693. https://doi.org/10.1016/S1364-6826(00)00029-8

Forbes, J. M., & Wu, D. (2006). Solar tides as revealed by measurements of mesosphere temperature by the MLS experiment on UARS. *Journal of the Atmospheric Sciences*, *63*(7), 1776–1797. https://doi.org/10.1175/JAS3724.1

Forbes, J. M., & Zhang, X. (2022a). Hough Mode Extensions (HMEs) and solar tide behavior in the dissipative thermosphere. *Journal of Geophysical Research: Space Physics*, *127*(11), e2022JA030962. https://doi.org/10.1029/2022JA030962

Forbes, J. M., & Zhang, X. (2022b). Thermosphere Hough Mode Extensions (HMEs) for solar tides in Earth's atmosphere [Dataset]. *Zenodo*. https://doi.org/10.5281/zenodo.7150798

Forbes, J. M., Zhang, X., Bruinsma, S., & Oberheide, J. (2011). Sun-synchronous thermal tides in exosphere temperature from CHAMP and GRACE accelerometer measurements. *Journal of Geophysical Research*, *116*(A11), A11309. https://doi.org/10.1029/2011JA016855

Forbes, J. M., Zhang, X., Palo, S., Russell, J., Mertens, C. J., & Mlynczak, M. (2008). Tidal variability in the ionospheric dynamo region. *Journal of Geophysical Research*, *113*(A2), A02310. https://doi.org/10.1029/2007JA012737

FORMOSAT-7/COSMIC-2 LASC and SWL Lab. (2024). Global ionospheric specifications. [Dataset]. Retrieved from http://formosat7.earth.ncku.edu.tw/

Hagan, M. E., & Forbes, J. M. (2002). Migrating and nonmigrating diurnal tides in the middle and upper atmosphere excited by tropospheric latent heat release. *Journal of Geophysical Research*, *107*(D24), ACL6-1–ACL6-15. https://doi.org/10.1029/2001JD001236

Harding, B. J., Chau, J. L., He, M., Englert, C. R., Harlander, J. M., Marr, K. D., et al. (2021). Validation of ICON-MIGHTI Thermospheric Wind Observations: 2. Green-line comparisons to specular meteor radars. *Journal of Geophysical Research: Space Physics*, *126*(3), e2020JA028947. https://doi.org/10.1029/2020JA028947

Häusler, K., Oberheide, J., Lühr, H., & Koppmann, R. (2013). The geospace response to nonmigrating tides. In F.-J. Lübken (Ed.), *Climate and Weather of the Sun-Earth System (CAWSES): Highlights from a priority program* (pp. 481–506). Springer Atmospheric Sciences. https://doi.org/10.1007/978-94-007-4348-9

ICON/MIGHTI Team. (2024). MIGHTI temperatures and green line winds. [Dataset]. Retrieved from https://icon.ssl.berkeley.edu/Data/Data-Product-Matrix

Jones, M., Jr., Forbes, J. M., Hagan, M. E., & Maute, A. (2014). Impacts of vertically propagating tides on the mean state of the ionosphere-thermosphere system. *Journal of Geophysical Research: Space Physics*, *119*(3), 2197–2213. https://doi.org/10.1002/2013JA019744

Khattatov, B. V., Yubin, V. A., Geller, M. A., Hays, P. B., & Vincent, R. A. (1997). Diurnal migrating tide as seen by the high-resolution Doppler imager/UARS: 1. Monthly mean global meridional winds. *Journal of Geophysical Research*, *102*(D4), 4405–4422. https://doi.org/10.1029/96JD03655

Kumari, K., & Oberheide, J. (2020). QBO, ENSO, and solar cycle effects in short-term nonmigrating tidal variability on planetary wave timescales from SABER—An information-theoretic approach. *Journal of Geophysical Research: Atmospheres*, *125*(6), e2019JD031910. https://doi.org/10.1029/2019JD031910

Lieberman, R. S., Oberheide, J., Hagan, M. E., Remsberg, E. E., & Gordley, L. L. (2004). Variability of diurnal tides and planetary waves during November 1978–May 1979. *Journal of Atmospheric and Solar-Terrestrial Physics*, *66*(6), 517–528. (Dynamics and Chemistry of the MLT Region - PSMOS 2002 International Symposium). https://doi.org/10.1016/j.jastp.2004.01.006

Lieberman, R. S., Oberheide, J., & Talaat, E. R. (2013). Nonmigrating diurnal tides observed in global thermospheric winds. *Journal of Geophysical Research: Space Physics*, *118*(11), 7384–7397. https://doi.org/10.1002/2013JA018975

Lieberman, R. S., Riggin, D. M., Ortland, D. A., Oberheide, J., & Siskind, D. E. (2015). Global observations and modeling of nonmigrating diurnal tides generated by tide-planetary wave interactions. *Journal of Geophysical Research: Atmospheres*, *120*(22), 11419–11437. https://doi.org/10.1002/2015JD023739

Lin, C.-Y., Lin, C. C.-H., Liu, J.-Y., Rajesh, P. K., Matsuo, T., Chou, M.-Y., et al. (2020). The early results and validation of FORMOSAT-7/COSMIC-2 space weather products: Global ionospheric specification and Ne-aided Abel electron density profile. *Journal of Geophysical Research: Space Physics*, *125*(10), e2020JA028028. https://doi.org/10.1029/2020JA028028

Lindzen, R. S., Hong, S. S., & Forbes, J. (1977). *Semidiurnal Hough mode extensions in the thermosphere and their application* (Tech. Rep. No. 3442). Naval Research Laboratory.

Liu, H.-L., Foster, B. T., Hagan, M. E., McInerney, J. M., Maute, A., Qian, L., et al. (2010). Thermosphere extension of the Whole Atmosphere Community Climate Model. *Journal of Geophysical Research*, *115*(A12), A12302. https://doi.org/10.1029/2010JA015586

Lu, X., Liu, A. Z., Oberheide, J., Wu, Q., Li, T., Li, Z., et al. (2011). Seasonal variability of the diurnal tide in the mesosphere and lower thermosphere over Maui, Hawaii (20.7°N, 156.3°W). *Journal of Geophysical Research*, *116*(D17), D17103. https://doi.org/10.1029/2011JD015599

Lu, X., Liu, H.-L., Liu, A. Z., Yue, J., McInerney, J. M., & Li, Z. (2012). Momentum budget of the migrating diurnal tide in the Whole Atmosphere Community Climate Model at vernal equinox. *Journal of Geophysical Research*, *117*(D7), D07112. https://doi.org/10.1029/2011JD017089

Maute, A., Forbes, J. M., Cullens, C. Y., & Immel, T. J. (2023). Delineating the effect of upward propagating migrating solar tides with the TIEGCM-ICON. *Frontiers in Astronomy and Space Sciences*, *10*, 1147571. https://doi.org/10.3389/fspas.2023.1147571

Mendillo, M., Rishbeth, H., Roble, R., & Wroten, J. (2002). Modelling F2-layer seasonal trends and day-to-day variability driven by coupling with the lower atmosphere. *Journal of Atmospheric and Solar-Terrestrial Physics*, *64*(18), 1911–1931. https://doi.org/10.1016/S1364-6826(02)00193-1

Murphy, D. J., Tsutsumi, M., Riggin, D. M., Jones, G. O. L., Vincent, R. A., Hagan, M. E., & Avery, S. K. (2003). Observations of a nonmigrating component of the semidiurnal tide over Antarctica. *Journal of Geophysical Research*, *108*(D8), ACL5.1–ACL5.11. https://doi.org/10.1029/2002JD003077

Oberheide, J. (2022). Day-to-day variability of the semidiurnal tide in the F-region ionosphere during the January 2021 SSW from COSMIC-2 and ICON. *Geophysical Research Letters*, *49*(17), e2022GL100369. https://doi.org/10.1029/2022GL100369

Oberheide, J., & Forbes, J. M. (2008). Tidal propagation of deep tropical cloud signatures into the thermosphere from TIMED observations. *Geophysical Research Letters*, *35*(4), L04816. https://doi.org/10.1029/2007GL032397

Oberheide, J., Forbes, J. M., Zhang, X., & Bruinsma, S. L. (2011a). Climatology of upward propagating diurnal and semidiurnal tides in the thermosphere. *Journal of Geophysical Research*, *116*(A11), A11306. https://doi.org/10.1029/2011JA016784

Oberheide, J., Forbes, J. M., Zhang, X., & Bruinsma, S. L. (2011b). Wave-driven variability in the ionosphere-thermosphere-mesosphere system from timed observations: What contributes to the "wave 4". *Journal of Geophysical Research*, *116*(A1), A01306. https://doi.org/10.1029/2010JA015911

Oberheide, J., Gardner, S. M., & Neogi, M. (2023). Resolving the tidal weather of the thermosphere using GDC. *Frontiers in Astronomy and Space Sciences*, *10*, 1282261. https://doi.org/10.3389/fspas.2023.1282261

Oberheide, J., Jones, M., Jr., & Kumari, K. (2023). Resolving the tidal weather of the thermosphere. *Bulletin of the AAS*, *55*(3), 300. Retrieved from https://baas.aas.org/pub/2023n3i300

Oberheide, J., Shihokawa, K., Gurubaran, S., Ward, W. E., Fujiwara, H., Kosch, M. J., et al. (2015). The geospace response to variable inputs from the lower atmosphere: A review of the progress made by Task Group 4 of CAWSES-II. *Progress in Earth and Planetary Science*, *2*(2), 2. https://doi.org/10.1186/s40645-014-0031-4

Oberheide, J., Wu, Q., Killeen, T., Hagan, M., & Roble, R. (2007). A climatology of nonmigrating semidiurnal tides from TIMED Doppler Interferometer (TIDI) wind data. *Journal of Atmospheric and Solar-Terrestrial Physics*, *69*(17), 2203–2218. https://doi.org/10.1016/j.jastp.2007.05.010

Oberheide, J., Wu, Q., Killeen, T. L., Hagan, M. E., & Roble, R. G. (2006). Diurnal nonmigrating tides from TIMED Doppler Interferometer wind data: Monthly climatologies and seasonal variations. *Journal of Geophysical Research*, *111*(A10), A10S03. https://doi.org/10.1029/2005JA011491

Pedatella, N. M., Forbes, J. M., & Oberheide, J. (2008). Intra-annual variability of the low-latitude ionosphere due to nonmigrating tides. *Geophysical Research Letters*, *35*(18), L18104. https://doi.org/10.1029/2008GL035332

Pedatella, N. M., & Harvey, V. L. (2022). Impact of strong and weak stratospheric polar vortices on the mesosphere and lower thermosphere. *Geophysical Research Letters*, *49*(10), e2022GL098877. https://doi.org/10.1029/2022GL098877

Pedatella, N. M., Oberheide, J., Sutton, E. K., Liu, H.-L., Anderson, J. L., & Raeder, K. (2016). Short-term nonmigrating tide variability in the mesosphere, thermosphere, and ionosphere. *Journal of Geophysical Research: Space Physics*, *121*(4), 3621–3633. https://doi.org/10.1002/2016JA022528

Pedatella, N. M., Richmond, A. D., Maute, A., & Liu, H.-L. (2016). Impact of semidiurnal tidal variability during SSWs on the mean state of the ionosphere and thermosphere. *Journal of Geophysical Research: Space Physics*, *121*(8), 8077–8088. https://doi.org/10.1002/2016JA022910

Rajesh, P. K., Lin, C. C. H., Lin, J.-T., Lin, C.-Y., Yue, J., Matsuo, T., et al. (2021). Day-to-day variability of ionospheric electron density during solar minimum derived from FORMOSAT-7/COSMIC-2 measurements. *Terrestrial, Atmospheric and Oceanic Sciences*, *32*(6.1), 1–17. https://doi.org/10.3319/TAO.2021.08.01.01

Richmond, A. D., Ridley, E. C., & Roble, R. G. (1992). A thermosphere/ionosphere general circulation model with coupled electrodynamics. *Geophysical Research Letters*, *19*(6), 601–604. https://doi.org/10.1029/92GL00401

Roble, R. G., & Ridley, E. C. (1994). A thermosphere-ionosphere-mesosphere-electrodynamics general circulation model (time-GCM): Equinox solar cycle minimum simulations (30–500 km). *Geophysical Research Letters*, *21*(6), 417–420. https://doi.org/10.1029/93GL03391

Roble, R. G., Ridley, E. C., Richmond, A. D., & Dickinson, R. E. (1988). A coupled thermosphere/ionosphere general circulation model. *Geophysical Research Letters*, *15*(12), 1325–1328. https://doi.org/10.1029/GL015i012p01325

van der Meeren, C., Laundal, K. M., Burrell, A. G., Lamarche, L. L., Starr, G., Reimer, A. S., & Morschhauser, A. (2023). aburrell/apexpy: Apexpy version 2.0.1 [Software]. *Zenodo*. https://doi.org/10.5281/zenodo.7818719

Vitharana, A., Zhu, X., Du, J., Oberheide, J., & Ward, W. E. (2019). Statistical modeling of tidal weather in the mesosphere and lower thermosphere. *Journal of Geophysical Research: Atmospheres*, *124*(16), 9011–9027. https://doi.org/10.1029/2019JD030573

Wang, J. C., Palo, S. E., Liu, H.-L., & Siskind, D. E. (2021). Day-to-day variability of diurnal tide in the mesosphere and lower thermosphere driven from below. *Journal of Geophysical Research: Space Physics*, *126*(2), e2019JA027759. https://doi.org/10.1029/2019JA027759

Yamazaki, Y., Harding, B. J., Qiu, L., Stolle, C., Siddiqui, T. A., Miyoshi, Y., et al. (2023). Monthly climatologies of zonal-mean and tidal winds in the thermosphere as observed by ICON/MIGHTI during April 2020–March 2022. *Earth and Space Science*, *10*(6), e2023EA002962. https://doi.org/10.1029/2023EA002962

Yuan, T., She, C. Y., Oberheide, J., & Krueger, D. A. (2014). Vertical tidal wind climatology from full-diurnal-cycle temperature and Na density lidar observations at Ft. Collins, CO (41°N, 105°W). *Journal of Geophysical Research: Atmospheres*, *119*(8), 4600–4615. https://doi.org/10.1002/2013JD020338